



Article

From Magneto-Dielectric Biocomposite Films to Microstrip Antenna Devices

Fernando Lima de Menezes ¹, Davino Machado Andrade Neto ^{1,2},
Maria do Livramento Linhares Rodrigues ³, Helder Levi Silva Lima ⁴,
Denis Valony Martins Paiva ³, Marcelo Antônio Santos da Silva ⁵,
Lillian Maria Uchôa Dutra Fechine ¹, Antônio Sérgio Bezerra Sombra ⁵, Rafael Melo Freire ⁶,
Juliano Casagrande Denardin ⁷, Morsyleide de Freitas Rosa ⁸,
Men de Sá Moreira de Souza Filho ⁸, Selma Elaine Mazzetto ⁹ and
Pierre Basílio Almeida Fechine ^{1,*}

¹ Group of Chemistry of Advanced Materials (GQMat)–Department of Analytical Chemistry and Physic-Chemistry, Federal University of Ceará–UFC, Pici Campus, 12100, CP 60451-970 Fortaleza, CE, Brazil; fdolime@gmail.com (F.L.d.M.); davinomachado@gmail.com (D.M.A.N.); dutralillian@gmail.com (L.M.U.D.F.)

² Federal Institute of Education, Science and Technology of Ceará—Campus Camocim, CP 62400-000 Camocim, CE, Brazil

³ Department of Organic and Inorganic Chemistry–Federal University of Ceará–UFC, Pici Campus, CP 60455-760 Fortaleza, CE, Brazil; marialinhairesr@hotmail.com (M.d.L.L.R.); valonydenis@gmail.com (D.V.M.P.)

⁴ Department of Chemical Engineering–Federal University of Ceará–UFC, Pici Campus, CP 60455-760 Fortaleza, CE, Brazil; helderlevi@gmail.com

⁵ Laboratory of Telecommunications and Science and Materials Engineering (LOCEM)–Department of Physics, Federal University of Ceará–UFC, Pici Campus, 12100, CP 60451-970 Fortaleza, CE, Brazil; marceloassilva@yahoo.com.br (M.A.S.d.S.); asbsombra@gmail.com (A.S.B.S.)

⁶ Institute of Applied Chemical Sciences, Universidad Autónoma de Chile, Santiago 8910060, Chile; rafael.m.freire@gmail.com

⁷ Departamento de Física/CEDENNA, Universidad de Santiago de Chile, USACH, Av. Ecuador 3493, Santiago 9170124, Chile; jcdenardin@gmail.com

⁸ Embrapa Agroindústria Tropical, Planalto do Pici, CP 60511-110 Fortaleza, CE, Brazil; morsyleide.rosa@embrapa.br (M.d.F.R.); men.souza@embrapa.br (M.d.S.M.d.S.F.)

⁹ Laboratory of Products and Process Technology (LPT), Department of Organic and Inorganic Chemistry, Federal University of Ceará–UFC, Pici Campus, 12100, CP 60451-970 Fortaleza, CE, Brazil; selma@ufc.br

* Correspondence: fechine@ufc.br; Tel.: +55-(85)-3366-9047

Received: 4 September 2020; Accepted: 21 September 2020; Published: 24 September 2020



Abstract: Magneto-dielectric composites are interesting advanced materials principally due to their potential applications in electronic fields, such as in microstrip antennas substrates. In this work, we developed superparamagnetic polymer-based films using the biopolymeric matrices chitosan (Ch), cellulose (BC) and collagen (Col). For this proposal, we synthesized superparamagnetic iron oxide nanoparticles (SPIONs) functionalized with polyethyleneimine with a cheap method using sonochemistry. Further, the SPIONs were dispersed into polymer matrices and the composites were evaluated regarding morphology, thermal, dielectric and magnetic properties and their application as microstrip antennas substrates. Microscopically, all tested films presented a uniform dispersion profile, principally due to polyethyleneimine coating. Under an operating frequency (f_0) of 4.45 GHz, Ch, BC and Col-based SPION substrates showed moderate dielectric constant (ϵ') values in the range of 5.2–8.3, 6.7–8.4 and 5.9–9.1, respectively. Furthermore, the prepared films showed no hysteresis loop, thereby providing evidence of superparamagnetism. The microstrip antennas showed considerable bandwidths (3.37–6.34%) and a return loss lower than -10 dB. Besides, the f_0 were modulated according to the addition of SPIONs, varying in the range of 4.69–5.55, 4.63–5.18 and 4.93–5.44 GHz,

for Ch, BC and Col-based substrates, respectively. Moreover, considering best modulation of ϵ' and f_o , the Ch-based SPION film showed the most suitable profile as a microstrip antenna substrate.

Keywords: biopolymers; magnetic-dielectric property; nanocomposites; microstrip antennas

1. Introduction

In recent years, with the advancement of technology in the device electronics field, the demand for new materials has grown, with increased focus on the development of light, flexible, biocompatible and high efficiency/volume ratio electrical components that are also compatible with the competitive and demanding market [1–4]. In this regard, polymer-ceramic composites have shown numerous advantages over ceramic bulks, where can present lower energy-consuming, easier molding and greater integration in manufacture of circuits [5–7]. For instance, in telecommunication industry focusing on the nanoscale range, hybrid nanocomposites have been widely requested as dielectric substrates [8], which must have low dielectric permittivity (ϵ') (between 2–12) and low dielectric loss ($\tan \delta$) [5]. On the other hand, materials with high dielectric permittivity (ϵ) have been applied in miniaturization of electronic radiator components [2,9], which causes problems such as bandwidth narrowing, low radiation efficiency and mutual coupling [1,10]. In this context, magnetic-dielectric materials with high ϵ' and magnetic permeability (μ) have been used to overcome these problems [11].

Magnetic nanoparticles dispersed into polymer matrix have shown a positively contribution for a high permeability (μ) behavior, while also allowing the reduction of the size of microstrip antennas without reducing their performance. According to the literature, magnetic nanoparticles, generally Fe, Fe_3O_4 , CoFe_2O_4 , $\text{Y}_3\text{Fe}_5\text{O}_{12}$, $\text{NiZnFe}_2\text{O}_4$, $\text{Mn}_x\text{Zn}_{(1-x)}\text{Fe}_2\text{O}_4$ and $\text{Ba}_{12}\text{Fe}_{28}\text{Ti}_{15}\text{O}_{84}$, are usually dispersed in a viscoelastic matrix, such as polydimethylsiloxane (PDMS) [2], polyvinyl alcohol [1], polystyrene [12], commercial Rogers[®] polymer [6,13], chitosan/gelatin [14], galactomannan [15], collagen [12,16] and polyvinylidene fluoride [17]. For example, a Fe_3O_4 /PDMS magnetic-dielectric composite could effectively improve the bandwidth and the yields with an adjustable dielectric property, and could also lower dielectric and magnetic loss under a magnetic field [6,11,18,19]. Indeed, Fe_3O_4 nanoparticles applied in magneto-dielectric substrates became very attractive, mostly due to their superparamagnetic property, which prevents losses through hysteresis and eddy current induction, with easy and low-cost obtention. However, it is always a challenge to synthesize superparamagnetic iron oxides (SPIONs) with high magnetization, since reducing their size increases oxidation, and consequently decreases magnetization [2].

In this context, an inorganic-organic core-shell architecture would provide more air-stable and monodisperse SPIONs, and consequently a more uniform dispersion into polymer matrices [13,20,21]. For example, molecules as oleylamine and poly(amido-amine) dendrimers have been used in surface coating procedures of Fe_3O_4 NPs showing nanocomposites with good homogeneity [18,20], while CoFe_2O_4 @oleylamine NPs have also provided uniform dispersion in a Rogers[®] polymer matrix [13].

In this work, we developed magneto-dielectric composites based on SPIONs coated with branched-polyethylenimine (bPEI) and involving further dispersion into three different biopolymer matrices: chitosan, collagen and cellulose, which present viscoelastic properties and large bioavailability. After standard characterization, the proposed magneto-dielectric film-form composites were successfully analyzed regarding their magnetic and dielectric losses, and were evaluated in terms of the reflection coefficient S_{11} , to show good bandwidths from 3.37% to 6.34% and a high return loss, which make them suitable for microstrip antennas applications.

2. Materials and Methods

2.1. Biopolymers Obtention

Low molecular weight chitosan (degree of deacetylation 75–85%, $M_w = 50,000\text{--}190,000$ Da) was purchased from Sigma–Aldrich and used without any previous purification procedure. Collagen was extracted from Nile Tilapia skins according to Sun and their co-worker's methodology with some modification. Previously, the skins were treated with $0.1\text{ mol}\cdot\text{L}^{-1}$ of NaOH in order to remove non-collagenous proteins, and washed with ethanol to remove lipids. Then, the skin was treated in $0.7\text{ mol}\cdot\text{L}^{-1}$ of acetic acid under stirring for 24 h for collagen extraction. Further, the extracted collagen was purified and freeze-dried under vacuum for adequate storage [22]. Nanofibrillated bacterial cellulose was kindly donated and obtained according to a previous published methodology that was well-reported by Lima and their co-workers [23]. Briefly, *Komagataeibacter xylinus* ATCC 53,582 was statically cultured in Hestrin and Schramm (HS) medium [24] at pH 6.0 and $30\text{ }^\circ\text{C}$ for 10 days, then the obtained cellulose membranes were washed with hot water ($90\text{ }^\circ\text{C}$), following immersion into an alkaline solution ($1\text{ mol}\cdot\text{L}^{-1}$ NaOH and 1% H_2O_2 *v/v*) at $80\text{ }^\circ\text{C}$ for 1 h. Subsequently, the membranes were rinsed with distilled water until a pH of 7.0 was obtained, and then were dried at $50\text{ }^\circ\text{C}$ for 48 h. Further, 1 g of grounded membrane was suspended into 100 mL of $1\text{ mmol}\cdot\text{L}^{-1}$ solution of 2,2,6,6-tetramethylpiperidinyloxy (TEMPO) and $10\text{ mmol}\cdot\text{L}^{-1}$ of KBr. Then, 5 mmol of NaClO were added to previously prepared suspension, under stirring (500 rpm) at $25\text{ }^\circ\text{C}$, and the pH was adjusted to 10. After 2 h of stirring, the suspension was washed until it reached a pH of 7.0 and mechanically treated in high-speed blender (25,000 rpm, in three cycles of 10 min). All obtained biopolymers were further used as a polymer matrix in the preparation of film-form composites.

2.2. Synthesis of SPIONs

The SPIONs were prepared by using a three-step synthesis, which was adapted according to the well-established ultrasound-assisted co-precipitation method [25]. Initially, a solution containing 1.16 g of $\text{FeSO}_4\cdot 7\text{H}_2\text{O}$ (Vetec Química, Rio de Janeiro, Brazil) and 1.85 g of $\text{FeCl}_3\cdot 6\text{H}_2\text{O}$ (Vetec Química, Rio de Janeiro, Brazil) in 15 mL of deionized water was sonicated for 4 min using an ultrasonic disruptor (Eco-Sonic QR750, 750 W, 20 kHz; Ultronique, São Paulo, Brazil), under an amplitude of 90%. Subsequently, 7.5 mL of 27% *w/w* ammonium hydroxide (Synth) were added under ultrasound irradiation during 4 min. Finally, 4.5 mL of a solution, briefly prepared by addition of 1.0 g of branched-polyethylenimine (bPEI) (Sigma-Aldrich, St. Louis, MO, USA, $M_w = 25,000$) in 4 mL of deionized water, were added into the reactional system. After 4 min of ultrasound irradiation, the functionalized SPIONs (referred to as $\text{Fe}_3\text{O}_4\text{@bPEI}$) were obtained. In order to remove the excess of remaining chemicals, the SPIONs were washed with deionized water and then redispersed in water and centrifuged at 3000 rpm for 10 min. The free-aggregate ferrofluid supernatant was collected and diluted in deionized water to $40\text{ mg}\cdot\text{g}^{-1}$ (SPIONs *w/w*).

2.3. Composite Films Preparation

The composite films were prepared by casting previously prepared $\text{Fe}_3\text{O}_4\text{@bPEI}$ ferrofluid into the polymer matrix at different proportions (0%, 30%, 50% and 80% of $\text{Fe}_3\text{O}_4\text{@bPEI}$ to matrix mass), as shown in Figure 1. As each polymer has a chemically different structure, a film preparation procedure was developed according to each polymer's specificity. For Col-based films, a solution containing collagen (3% *w/v*) was prepared in acetic acid (3% *w/w*, Merck, Kenilworth, NJ, USA) and then glycerol (GL) (Vetec Química, Rio de Janeiro, Brazil) was added at a proportion of 20% *w/w* to collagen mass, in order to provide greater flexibility to the films. Afterwards, we added $\text{Fe}_3\text{O}_4\text{@bPEI}$ $40\text{ mg}\cdot\text{g}^{-1}$ at different proportions and stirred for 15 min. Thereafter, the final dispersion was degassed under vacuum to remove air-bubbles, transferred to Petri dishes and dried at room temperature.

For Ch-based films, a chitosan solution (2% *w/v*) was prepared in 20 mL of acetic acid (2% *w/w*). Then, GL (20% *w/w*) was added to the previously prepared chitosan solution and sonicated in an

ultrasonic disruptor using a 13 mm probe for 3 min under an amplitude of 60%. Prior to sonication, Fe₃O₄@bPEI ferrofluid was added to the film-forming suspension in the desired amounts. Furthermore, the dispersion was degassed, and 20 g were transferred to Petri dishes and dried at room temperature.

For BC-based films, a suspension of nanofibrillated bacterial cellulose was prepared in 35 mL of water (1% w/v). Then, GL was added into BC suspension in the proportion of 25% w/w to cellulose mass, slightly higher than other matrices, in order to avoid brittle and poor mechanical strength films. Then, the mixture was stirred for 1 h and sonicated in an ultrasonic disruptor using a 13 mm probe for 3 min under an amplitude of 60%. Finally, the suspension was degassed, transferred to Petri dishes and dried at 70 °C in an air circulation oven. As for Ch-based films preparation, Fe₃O₄@bPEI ferrofluid was added at different amounts prior to the ultrasonic step.

At this point, 12 different composite films were prepared using collagen (Col), chitosan (Ch) and cellulose (BC) as a biopolymer matrix, where their amount parameter differences are presented in Table 1.

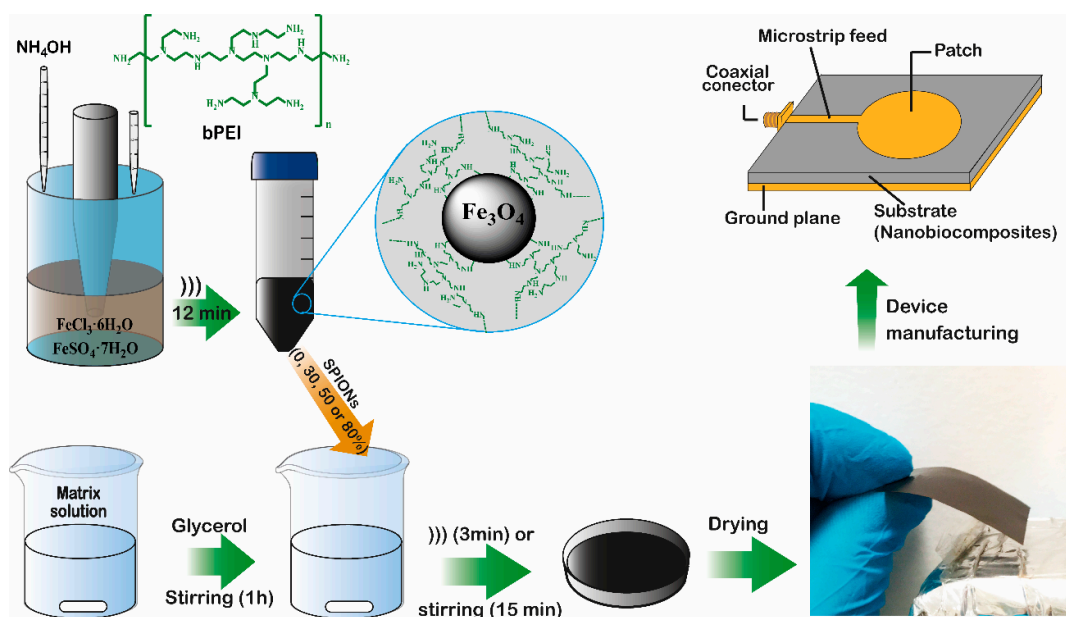


Figure 1. Representative illustration of biocomposite films preparation.

Table 1. Composition and thickness of prepared magneto-dielectric biocomposite films.

| Samples | GL (%) | SPION (%) | Thickness (µm) |
|---------|--------|-----------|----------------|
| Ch0 | 20 | 0 | 88 |
| Ch30 | 20 | 30 | 67 |
| Ch50 | 20 | 50 | 61 |
| Ch80 | 20 | 80 | 66 |
| Col0 | 20 | 0 | 43 |
| Col30 | 20 | 30 | 127 |
| Col50 | 20 | 50 | 148 |
| Col80 | 20 | 80 | 155 |
| BC0 | 25 | 0 | 29 |
| BC30 | 25 | 30 | 47 |
| BC50 | 25 | 50 | 54 |
| BC80 | 25 | 80 | 65 |

2.4. Characterization

X-ray Diffraction (XRD) and Fourier Transform Infrared Spectroscopy (FTIR) analysis were performed to study the structure of both Fe₃O₄@bPEI nanoparticles and the prepared film-form

composites. The samples were analyzed by using XRD in the range 10° – 80° , using a Bruker D8 Advance diffractometer (Bruker AXS, Billerica, MA, USA) operating in a 40 kV voltage and a 40 mA current with $\text{CuK}\alpha 1$ radiation ($\lambda = 0.154$ nm). Crystalline phases were identified using the ICSD database. FTIR spectra were obtained in the range 4000 – 400 cm^{-1} from the macerated film (in KBr pellets) using a Bruker spectrometer (FT-IR VERTEX 70V, Bruker Optics, Billerica, MA, USA).

A Scanning Electron Microscope (SEM) Inspect S50 FEI Instrument was used in order to analyze the morphology and dispersion of SPIONs into composite films. In order to avoid films tearing during measurements, the experiment was conducted using an electron beam of 20 kV with different magnification levels ($500\times$ for EDS measurements, $12,000\times$ for film-form collagen-less resistant-and $22,000\times$ for the other films).

Thermogravimetric analysis was performed to determine the decomposition temperature of the samples using 5.3 mg of each sample in a Mettler Toledo TGA/SDTA 851e instrument with a N_2 flow (50 $\text{cm}^3\cdot\text{min}^{-1}$), heating rate of 10 $^{\circ}\text{C}/\text{min}$ and temperature range of 30 – 900 $^{\circ}\text{C}$.

The magneto-dielectric biocomposite films were also analyzed regarding microwave dielectric properties by using Kent's cavity perturbation method [26,27], which involved using a Vector Network Analyzer (Agilent N5230C, Agilent Technologies, Santa Clara, CA, USA) and a harmonic coaxial split-cavity with a 0.4 to 4.5 GHz resonant frequency range; magnetic properties were analyzed using a Vibrating Sample Magnetometer (Cryogenic VSM 5 T system, Cryogenic Limited, London, UK) under a magnetic field of up to ± 7 kOe at room temperature.

Prototypes of the microstrip antennas were designed and manufactured using a conductive silver tape stick for a rectangular and circular form-type. The rectangular ground plane (30×25 mm^2) and the circular patch (diameter 13 mm) of prototype are shown in Figure 1. Circular and rectangular electrodes were connected to a coaxial SMA connector (50 ohm) using a microstrip (length of 10.6 mm) to feed the patch. The dimensions of these components were chosen according to devices operating at around 5.0 GHz. These antennas were characterized using a Vector Network Analyzer (Agilent N5230C).

3. Results

3.1. Microstructural Analysis

The synthesis of the $\text{Fe}_3\text{O}_4@b\text{PEI}$ NPs used in this work was performed according to a protocol recently published by our group [25], with an extensive characterization, including its structural, morphological, magnetic, colloidal and relaxivity properties. As already reported, $\text{Fe}_3\text{O}_4@b\text{PEI}$ NPs were successfully obtained with a cubic structure of inverse spinel (Fd3m) and an average crystallite size of around 10.2 ± 0.2 nm, where bPEI coating provided a well-stable ferrofluid with surface positively charged particles of around $+44.5 \pm 6.0$ mV and an average hydrodynamic radius in the range of 109.1 ± 5.0 nm, as well as a polydispersity index value of 0.060 ± 0.018 compared to monodisperse systems. Indeed, all these colloidal parameter results were very attractive for using $\text{Fe}_3\text{O}_4@b\text{PEI}$ NPs as a filler in a polymer matrix, giving the possibility to explore and develop a "new-generation" of biocomposites for antenna applications. Therefore, this work will focus on the characterization discussion of prepared magneto-dielectric composite films using different matrices, as illustrated in Figure 1.

3.1.1. XRD

Figure 2 shows XRD patterns obtained for all prepared biocomposite films and $\text{Fe}_3\text{O}_4@b\text{PEI}$ NPs. All films (Figure 2a–c) showed diffraction peaks at $2\theta = 18.6^{\circ}$, 30.3° , 35.6° , 43.3° , 53.7° , 57.3° , 62.8° and 74.7° , which can be indexed to (111), (220), (311), (400), (422), (511), (440) and (533) planes of the cubic spinel structure of magnetite, respectively, according to JCPDS file no. 01-088-0315, as shown in Figure 2d.

For Ch-based films, in all proportions (Figure 2a), XRD patterns presented a peak at $2\theta = 11.5^{\circ}$ attributed to hydrated chitosan crystals, a weak peak at 15.1° assigned to a very small amount of the

anhydrous crystals, a peak at 18.1° related to the presence of regular crystal lattice of the matrix and a broad peak around of 21° indicating the existence of an amorphous structure, according to JCPDS file no. 00-040-1521 [28–30]. Indeed, as observed for Ch0 film (Figure 2d), the Ch-based composites also had an amorphous halo, which is related to chitosan fragments with no long-range ordering, and becomes less intense as the SPIONs content increases. It was also noticed that the characteristic peaks of chitosan decrease in intensity when the magnetite increment increases into the matrix. Although the peak at $2\theta = 18^\circ$ can be also assigned to the magnetite lattice, its relative intensity did not increase with the SPIONs increment. Actually, the opposite behavior was observed, indicating the predominant contribution of chitosan for this diffraction. Interestingly, the intensity for this peak was greater than that observed at $2\theta = 21^\circ$, indicating that there was an improvement in the crystalline order of the matrix in the composites, which could be related to the ultrasonic treatment in the films.

A broad peak at $2\theta = 20.8^\circ$ was also observed in Col-based films (Figure 2b,d), which can be assigned to diffuse scattering in many layers of collagen fibers, and which characterizes a single left-handed helix chain [22]. The composites also presented a halo, related to the amorphous phases of the collagen matrix.

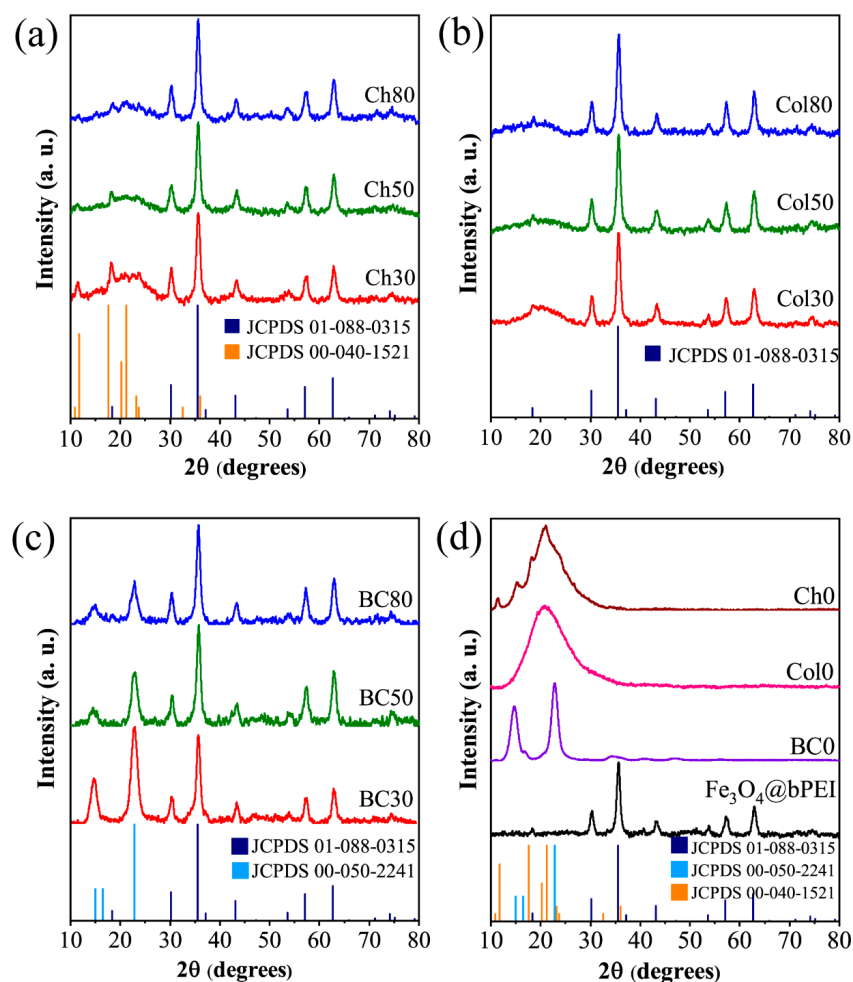


Figure 2. X-ray patterns of (a) Chitosan films; (b) Collagen films; (c) Bacterial cellulose films; and (d) Pure components of biocomposite films.

Peaks at $2\theta = 14.6^\circ$, 16.8° and 22.8° were observed to BC-based composites and assigned to (101), $(10\bar{1})$ and (002) planes, respectively, according to JCPDS file 00-50-2241 (Figure 2d). The sharp peaks (101) and (002) indicate the high crystallinity of BC in the film-form (0.773 on the Segal crystallinity index [31]), which is in agreement with results found in other studies [32,33]. Indeed, for BC-based

films in all proportions, the peaks observed in the XRD patterns are characteristics of cellulose type I-alpha with a triclinic unit cell, according to the Z-discriminant function proposed by Wada and Okano [34]. This polymorph is predominant in cellulose produced by bacteria [33]. In addition, the absence of peaks at $2\theta = 12^\circ$ or 20° in composites, related to type II cellulose, indicates that the film-formation method did not change the crystalline phase of the polymer [35].

3.1.2. FTIR

The infrared spectra for all composites and their single components are presented in Figure 3. All Ch films (Figure 3a) showed a wide band centered at 3286 cm^{-1} assigned to hydrogen bonds in $-\text{OH}$ groups, overlapped by contributions due to the symmetrical stretching of the amine N-H bonds [36]. Bands at 2920 , 2865 , 1405 and 1258 cm^{-1} were related to symmetrical and antisymmetrical C-H vibrations of CH_2 [37]. A small shoulder at 1632 cm^{-1} and the bands at 1554 and 1327 cm^{-1} can be associated to C=O stretching modes (amide I), N-H deformation modes (amide II) and C-N stretching modes (amide III), respectively [38,39]. The band near to 1026 cm^{-1} was assigned to stretching vibration C-O of ether and primary alcohol, and can be associated with the presence of glycerol and the piranosydic bonds of chitosan [14,40]. Additionally, the asymmetric stretching mode of the C-O-C bridge was observed at 1153 cm^{-1} [40].

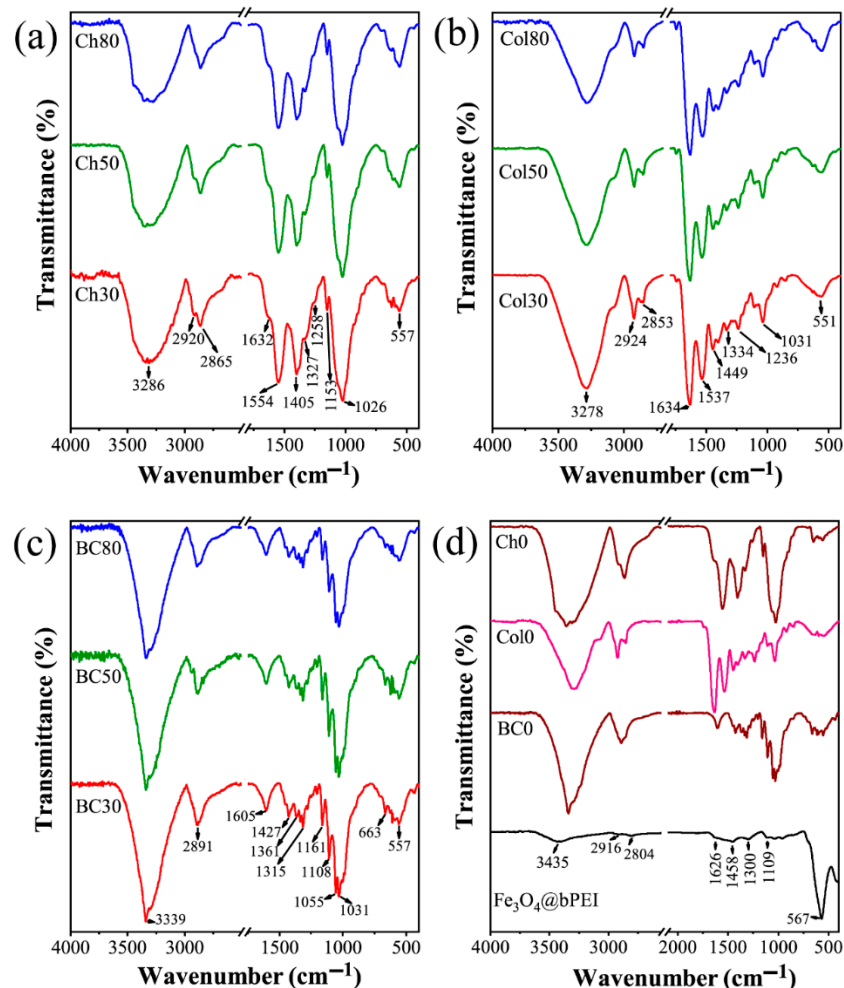


Figure 3. Fourier Transform Infrared Spectroscopy (FTIR) spectra of (a) Chitosan films; (b) Collagen films; (c) Bacterial cellulose films; and (d) Pure components of biocomposite films.

However, a spectral difference was noticed between Ch-based composites and film-form pure chitosan, where it is possible to observe that increasing magnetite content in the composite led to the

band at 557 cm^{-1} becoming more defined, which was assigned to Fe-O stretching modes at octahedral and tetrahedral sites in the SPIONs [40]. In this context, the progressive reduction in the intensity of the bands at 2920 , 1258 and 1327 cm^{-1} and the displacement of the bands at 1327 and 1258 cm^{-1} to higher wavenumbers were also observed, indicating strong interactions between amine groups on SPIONs surface and amide and hydroxymethyl groups from chitosan in the film [36].

All spectra of Col-based films (Figure 3b), including film-form pure collagen (Figure 3d), showed characteristic bands of amide A, amide B, amide I, amide II and amide III. The amide A band, assigned to N-H stretching with hydrogen bonds, was observed at 3278 cm^{-1} , while amide B band was observed at 2924 cm^{-1} , related to the asymmetric stretching C-H of CH_2 [22]. Amides I, II and III were observed at 1634 , 1537 and 1236 cm^{-1} , respectively, at lower frequencies than those reported by Chen et al. (2016), indicating the presence of stronger hydrogen bonds in the obtained films [41]. In these spectra, bands at 2853 , 1449 , 1334 and 1031 cm^{-1} can be related to symmetrical stretching CH_2 , to CH_2 bending, to CH_2 wagging of the proline and to C-O stretching from glycerol, respectively [42]. Fe-O stretching mode of magnetite was observed at 551 cm^{-1} , overlapped by a band due to skeletal stretching of collagen [42]. Additionally, the ratio of the intensities between 1236 and 1449 cm^{-1} bands with a value around 1 confirmed the maintenance of the triple helix of the collagen [41].

BC-based films spectra are shown in Figure 3c. Hydrogen bonds between cellulose molecules and O-H stretching were indicated by a 3339 cm^{-1} band. The bands at 2891 , 1427 and 1361 cm^{-1} were assigned to stretching and bending vibrations of CH, while the band at 1605 cm^{-1} , characteristic of carboxylate ions, confirmed the oxidation of cellulose when using TEMPO [33,43]. The existence of benzene ring mixed with the CH in-plane bending justified the band at 1315 cm^{-1} , while C-O-C antisymmetric stretching was evidenced in the band at 1161 cm^{-1} [33,44]. The bands at 1108 , 1055 , 1031 and 663 cm^{-1} were assigned, respectively, to C-C stretching of polysaccharide rings, C-O stretching, C-O bending of the C-OH of carbohydrates and C-OH out-of-plane bending vibrations [44]. Additionally, Fe-O vibration of magnetite was observed at 557 cm^{-1} and the reduction of 663 cm^{-1} band in the composites indicated strong cellulose-SPIONs interactions.

3.1.3. SEM

All SEM micrographs are shown in Figures S1–S3 in the Electronic Support Information (ESI). Figure 4 shows the SEM images only for Ch, Col and BC30 samples, i.e., composite films with 30% of SPIONs. Ch30 micrograph (Figure 4a) presented a typical granular surface, whereas in Col30 image (Figure 4d) wrinkles were observed, which could be formed during air-drying process due to the low mobility of film-form collagen matrix. BC30 image (Figure 4g) showed a fibrous structure where a relief surface was also observed. The SPIONs dispersion into biopolymer matrix for all samples was observed using Fe-mapping by Energy Dispersive Spectroscopy (EDS), as shown in Figure S3 (ESI). Figure 4c,f,i presents Fe mapping only for Ch, Col and BC30 samples. In general, all micrographs show well-dispersed Fe_3O_4 @bPEI NPs through the biopolymers matrix, where darker regions coincide with the relief on composites surface, indicating no clusters formation of SPIONs. Indeed, additional concerns can be taken in comparison to some works in the literature. For instance, in this work the use of a very stable colloidal dispersion SPION could provide well-distributed NPs throughout the polymer matrix, i.e., without any presence of agglomerates, which was not observed in other studies with $\text{Y}_3\text{Fe}_5\text{O}_{12}$ and $\text{NiZnFe}_2\text{O}_4$ using polymer matrices such as collagen, chitosan and galactomannan [14–16]. It is also interesting to mention that the better the NPs dispersion into composite, the greater the number of matrix-fill interfaces, and the greater the dielectric constant [45]. Furthermore, the filling agglomeration generates porous regions that easily trap moisture and increase undesired dielectric losses [46]. Another relevant advantage, considering the use of colloidal dispersions, is the apparently increase of mechanical strength resistance of the film towards fracture and high flexibility, even with high proportion of SPIONs in composite composition.

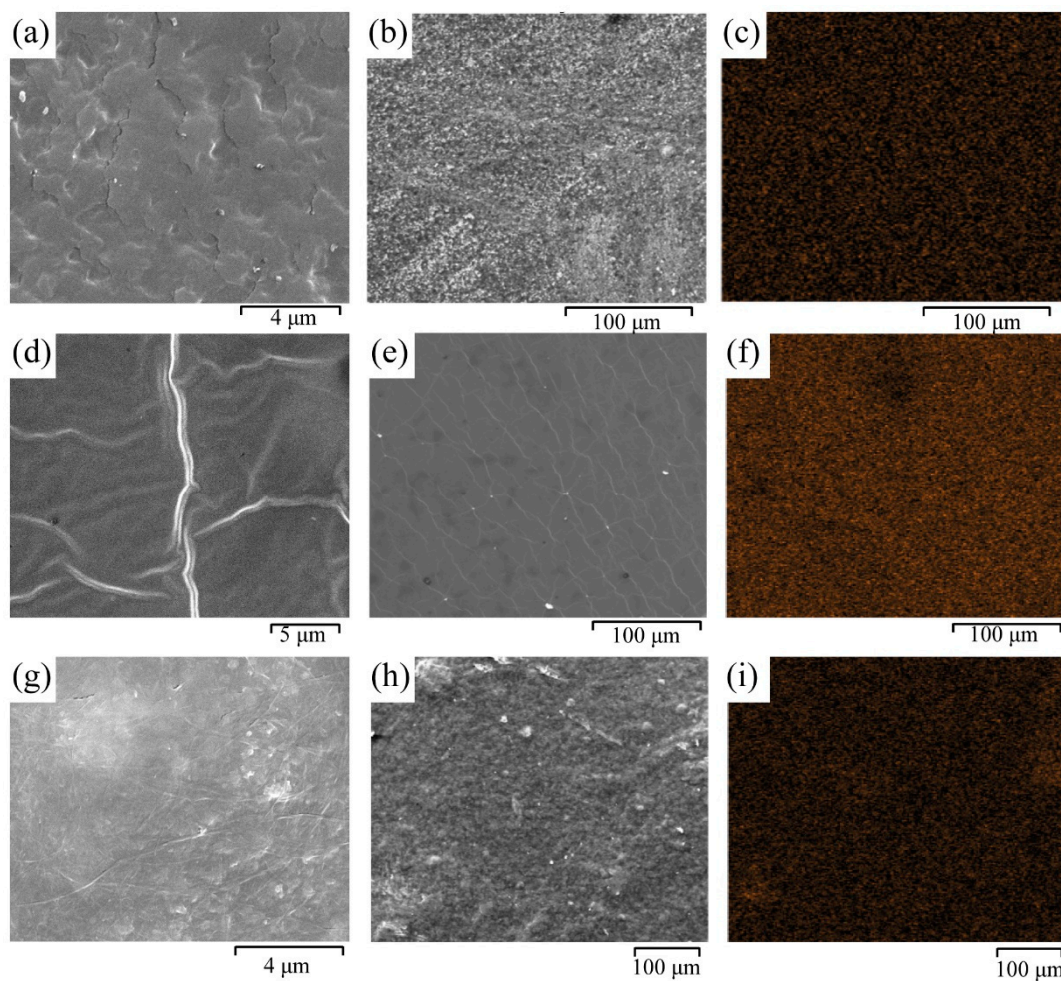


Figure 4. Micrographics and Fe mappings obtained by using Energy Dispersive Spectroscopy (EDS) for 30% superparamagnetic iron oxide nanoparticles (SPIONs) composites: (a–c) Ch30; (d–f) Col30; and (g–i) BC30.

3.2. Thermogravimetric Analysis

Thermogravimetric analysis (TGA) was performed to observe thermal degradation and to determine the relative weight loss of composite films. Figure 5 shows degradation curves of Ch, Col and BC80 composite films, i.e., biopolymer-based films with 80% of SPIONs, as well as pure biopolymers film-form and pure SPIONs. In addition, Table 2 shows all degradation events of each analyzed sample, where T^R is the event temperature range ($^{\circ}\text{C}$), T^M is maximum weight loss temperature ($^{\circ}\text{C}$), W^L is the weight loss (%) and R^W is the residual weight (%).

For analyzed composite samples at temperatures of up to $330\text{ }^{\circ}\text{C}$, Ch80 and Col80 showed lower weight loss, whereas Ch80 presented highest weight loss. Similar profiles were observed for pure matrix and composite films. However, all composite films proved to be more stable than their respective pure matrices. Interestingly, among analyzed composite films, Col80 had the slowest weight loss, which might be due to the thermal energy that is absorbed by the material in denaturation processes (melting processes), without accelerated formation of gaseous elements [47].

When considering first events, through derivative thermogravimetry (DTG) curves, all composites showed a T^R in the range from 30 to $125\text{ }^{\circ}\text{C}$, with T^M values at 52 , 55 and $60\text{ }^{\circ}\text{C}$ for Col80, BC80 and Ch80, respectively. These events were also observed in pure biopolymers film-form, which could be related to the moisture loss into matrices [16,40]. Indeed, the lower weight loss of composites indicates a reduced water affinity in comparison to their pure matrix films. However, Ch80 and Col80 samples proved to have more ability to retain water (see Table 2), which may be associated with

the presence of strong ion-dipole interactions between water and residual acetate in their structures. Although cellulose presents carboxylate groups in its structure, this is possibly linked to amine groups on SPION surfaces.

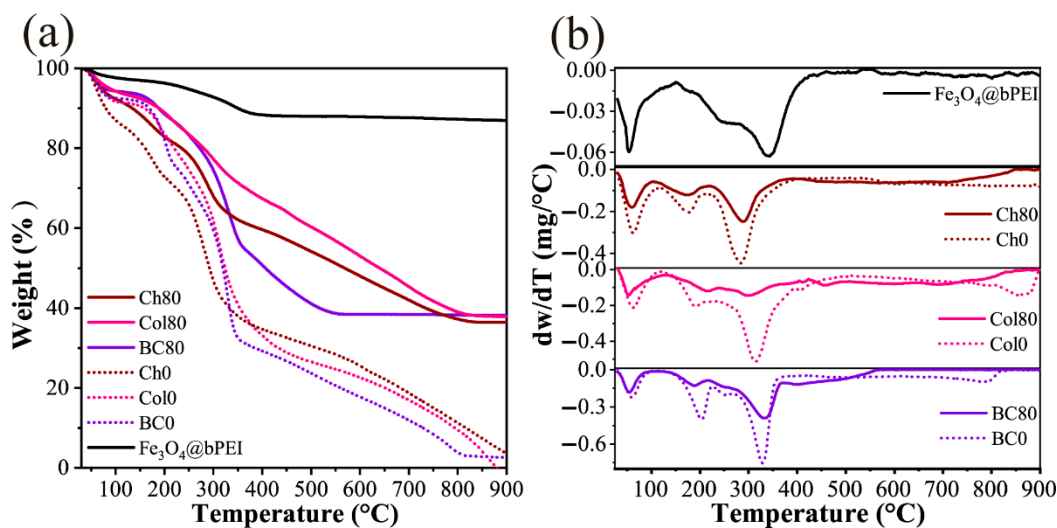


Figure 5. Decomposition curves of pure biopolymers film-form, composite films with 80% of SPIONs and Fe₃O₄@bPEI NPs: (a) thermogravimetric analysis (TGA) and (b) derivative thermogravimetry (DTG) curves.

Table 2. Degradation events for pure biopolymers film-form, composite films with 80% of SPIONs and Fe₃O₄@bPEI (SPIONs).

| Samples | 1st Event | | | 2nd Event | | | 3rd Event | | | R ^W |
|--------------------------------------|----------------|----------------|----------------|----------------|----------------|----------------|----------------|----------------|----------------|----------------|
| | T ^R | T ^M | W ^L | T ^R | T ^M | W ^L | T ^R | T ^M | W ^L | |
| Ch0 | 30–119 | 62 | 14.76 | 119–212 | 177 | 13.77 | 212–402 | 284 | 36.85 | 3.59 |
| Ch80 | 30–106 | 60 | 8.05 | 106–218 | 174 | 10.61 | 218–390 | 288 | 21.26 | 38.18 |
| Col0 | 30–119 | 62 | 8.64 | 119–233 | 191 | 13.66 | 233–500 | 315 | 51.16 | 0.16 |
| Col80 | 30–124 | 52 | 6.68 | 124–239 | 217 | 8.72 | 239–423 | 300 | 18.68 | 37.86 |
| BC0 | 30–108 | 60 | 7.57 | 108–224 | 203 | 17.16 | 224–375 | 329 | 44.71 | 2.61 |
| BC80 | 30–107 | 55 | 5.80 | 107–215 | 189 | 7.06 | 215–371 | 333 | 33.12 | 38.18 |
| Fe ₃ O ₄ @bPEI | 30–151 | 54 | 3.02 | 151–280 | 244 | 3.35 | 280–434 | 342 | 5.52 | 86.97 |

The second event, assigned to the loss of glycerol of composite films, showed T^M values at 173, 189 and 217 °C for Ch80, BC80 and Col80, respectively [48]. For Col80, a higher T^M was observed showing a better interaction between glycerol and Col80 film. According to Li and Li, besides glycerol generally promoting a better dissolution of aggregates into polymer matrix, it also increases the temperature of collagen denaturation due to formation of excimers of tyrosine residues [49]. Probably, these interactions complicate the weight loss of glycerol during the temperature range of the second event. However, this profile may only be related to Col0 film, i.e., when there is no presence of SPIONs, once the weight loss of glycerol is faster for Col80, when the formation of excimers is replaced by interactions between collagen and bPEI from SPIONs.

The third event occurs at T^M values of around 288, 300 and 333 °C, respectively, for Ch80, Col80 and BC80, which is related to the degradation of polymer chains of matrices and polyethyleneimine into composites (Figure 5b) [16,36,44]. Higher T^M values for Ch80 and BC80 composites indicate a greater thermal stability in comparison to their pure matrix-based films. It is also important to relate the significant contribution of bPEI to the higher thermal stability of all prepared biocomposite films, since the degradation curve for SPIONs (see Fe₃O₄@bPEI sample in Figure 5b and Table 2) showed a lower rate of weight loss.

3.3. Dielectric and Magnetic Properties

3.3.1. Microwave Dielectric Spectroscopy

The obtained data from microwave dielectric spectroscopy is shown in Figure 6. All results were determined while considering the thickness factor and performance of composites during each measurement.

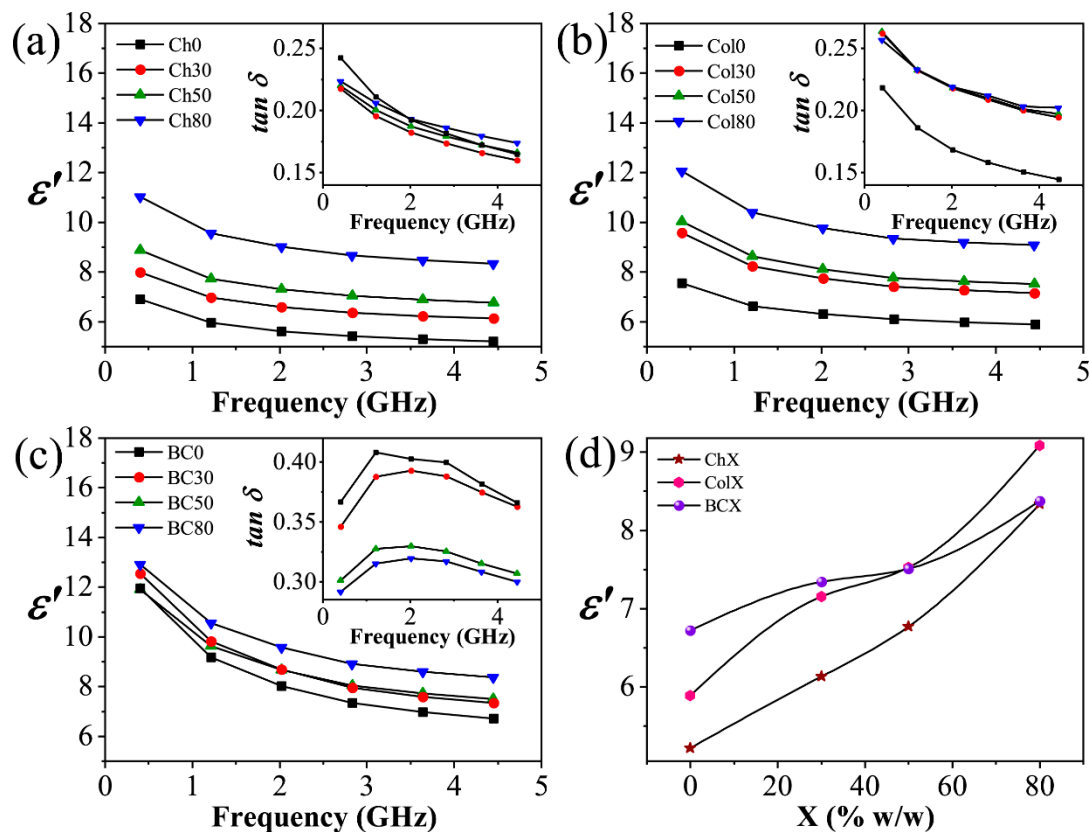


Figure 6. Variation of ϵ' and $\tan \delta$ (inset graph) of biocomposites with applied frequency: (a) Ch-based composite films; (b) Col-based composite films; and (c) BC-based composite films. (d) Variation of ϵ' at 4.45 GHz vs. X amount of SPIONs (% w/w) in the matrix.

In general, Ch-based composite films presented the lowest dielectric permittivity with ϵ' values of around 6.9–5.2 (Figure 6a), whereas Col-based films exhibited the lowest loss tangent with $\tan \delta$ values of around 0.218–0.145 (Figure 6b). These two different profiles can be attributed to the porosity structure of chitosan, as shown in SEM images, which may provide a more aerated film, with lower permittivity in comparison to a chitosan matrix. In addition, the low mobility of collagen chains contributes to these results. The ϵ' values for all composites significantly decrease with increasing frequency, and BC-based composite films present the greatest variation. This behavior is in accordance to those observed in other works for collagen and some polysaccharides [15,50,51], which can arise from the inability of the dipoles to become biocomposite films or reorient themselves when the direction of applied field changes more quickly [52]. In this work, using a frequency range of 0.4–4.5 GHz, dipolar orientation is the predominant mechanism of dielectric polarization and the greatest reduction in ϵ' values for BC-based composites suggests the lower mobility of the BC matrix in comparison to Ch and Col, as well as the dielectric relaxation process being related to the increase in $\tan \delta$ values.

Figure 6d shows the variation of ϵ' at 4.45 GHz with SPIONs content (0, 30, 50 and 80% w/w) in the matrix, which showed the dielectric property increasing by SPION increments into composite films, as recorded by Bibikov et al. (2013) [53]. Chemically, the resistive ceramic structure of Fe_3O_4 @bPEI NPs positively contributes to higher ϵ' values due to polar amine groups from bPEI molecules. However,

for BC-based films, ϵ' increases with the increasing of SPIONs content into a cellulose matrix, which was smaller than the other matrices (see the curve in Figure 6d), resulting in a different interaction-type between SPIONs and the cellulose matrix.

Specifically, for the cellulose matrix, the presence of both negatively (carboxylates from oxidized cellulose) and positively (protonated amines from SPIONs) charged species provided an electrostatic interaction between the molecules, which could reduce the mobility of these dipolar components under an electric field, consequently suppressing the expected increase regarding polarizability. For chitosan and collagen, the presence of larger cationic species with low mobility and smaller anions with high mobility provide a higher polarizability. Nevertheless, all obtained composites showed permittivity values in the range of $5.0 \leq \epsilon' \leq 9.0$, usually related to application as microstrip antenna substrates [54].

The applied-efficiency of biopolymer-based composite films as a substrate of microstrips is also governed by $\tan \delta$, which can indicate undesirable dissipation of electrical energy. These results are presented in the inset of Figure 6a–c. For chitosan and collagen-based films, although the higher contents of filler improves by ϵ' , this increasing can also increase dielectric losses, which can be explained by the increase of the number of interfaces between different materials [5]. However, the Ch30 sample showed a smaller $\tan \delta$ value when compared to Ch0, indicating that SPION may fill empty spaces, consequently improving the structural organization of the chitosan matrix, as indicated by XRD.

A different profile was observed for BC-based films, where higher amounts of SPIONs provided lower dielectric losses. Melone et al. reported the formation of crosslinking bonds between TEMPO-oxidized cellulose molecules with bPEI chains under thermic treatment, which may have decreased dielectric losses in this matrix [55]. Interestingly, cellulose composites showed a non-linear behavior of $\tan \delta$ with the frequency, which can be related to a specific relaxation process of the matrix. However, for application in microwave operating devices, even BC-based films with fewer dielectric losses are less advantageous than Col and Ch-based composites, which presented the lowest losses (less than 0.26).

3.3.2. Vibrating Sample Magnetometer

VSM results of all composite film samples and SPIONs are presented in Figure 7. Only a narrow hysteresis loop was observed for Fe_3O_4 @bPEI (Figure 7a), which evidences a nearly superparamagnetic behavior. Indeed, these results were already expected, since the full characterization of Fe_3O_4 @bPEI NPs used in this work were previously published by our group, where we provided an extensive magnetic characterization [25]. In addition, in that study we also proved through ZFC-FC analysis the superparamagnetism of Fe_3O_4 @bPEI NPs with no temperature blocking up to 300 K [25]. Indeed, the remanence observed in the measurements could be attributed to several factors, such as artificial broadening due to electric currents trapped in superconducting coil of the magnetometer, as well as interparticle polar interactions [25,56]. In fact, a decrease on remanence can be seen in the composites, mainly for Ch30 and Ch50 samples, indicating a reduction on the interparticle interactions related to a greater dispersion of SPIONs in the matrix. Actually, a superparamagnetic property is highly needed to achieve a magneto-dielectric profile in order to avoid losses induced by coercivity and Foucault's current, as previously mentioned [2].

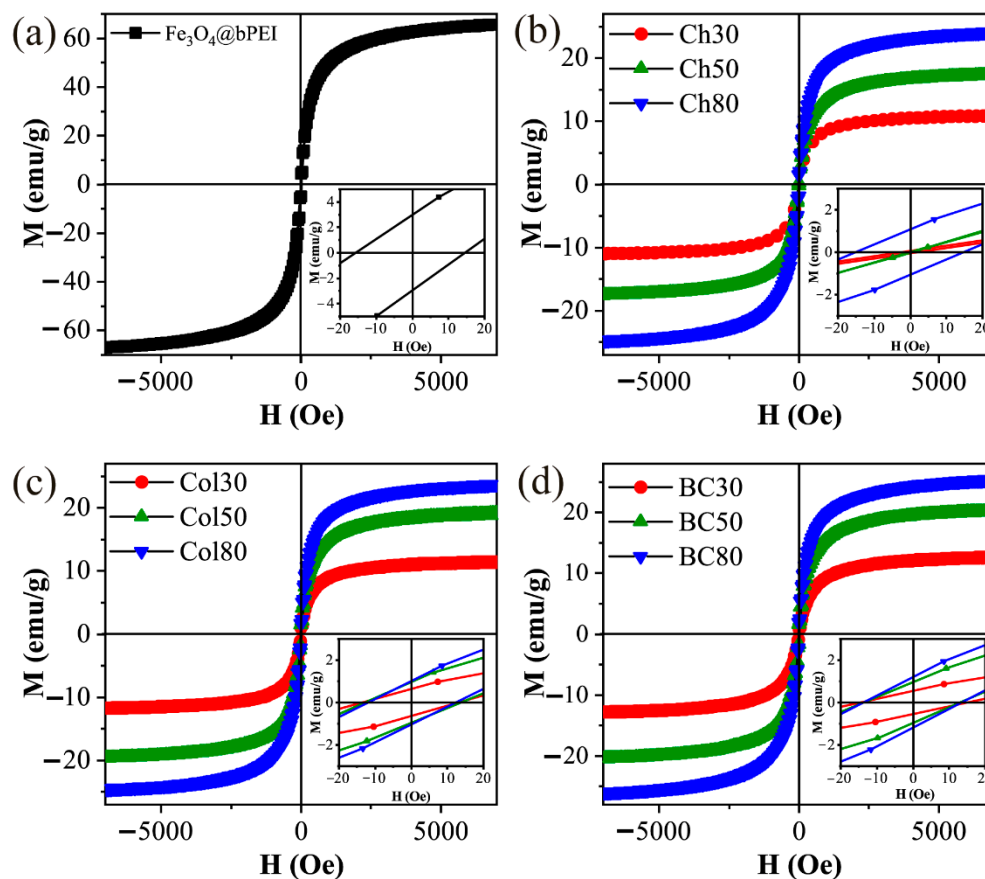


Figure 7. Magnetization curves of: (a) SPIONs; (b) Ch-based films; (c) Col-based films; and (d) BC-based films.

Figure 7b–d shows magnetization curves at room temperature for biopolymer-based composite films. As expected, the composites exhibited lower M_s values in comparison to $\text{Fe}_3\text{O}_4@b\text{PEI}$ with saturation magnetization (M_s) of 66.0 emu/g (Figure 7a). Ch-based films showed M_s values of 10.8, 17.4 and 24.3 emu/g for Ch30, Ch50 and Ch80, respectively, whereas Col-based composites presented M_s values around 11.5, 18.8 and 24.0 emu/g, and BC-based films 12.6, 19.8 and 25.5 emu/g, respectively from 30% to 80% of SPIONs in the films. However, it is possible to observe that M_s values are directly proportional to SPIONs content in the film composition. Actually, for each composite, the M_s value is close to one calculated by multiplying $\text{Fe}_3\text{O}_4@b\text{PEI}$ M_s value and its weight percentage in the films. For instance, BC30 has 30 mg of SPIONs for each 100 mg of bacterial cellulose and 25 mg of glycerol, approximately 19.3% w/w of $\text{Fe}_3\text{O}_4@b\text{PEI}$. Therefore, $M_{s\text{BC}30} = 19.3\% \times 66.0 \text{ emu/g} = 12.7 \text{ emu/g}$. This profile suggests that the films were formed by physical mixing only, which did not affect the structure and magnetic properties of SPIONs, as is also supported by FTIR and XRD results.

3.4. Design and Characterization of the Microstrip Patch Antennas

All prototypes of circular microstrip antennas (Figure 8) were developed with a patch diameter of 13 mm in a rectangular substrate of $30 \times 25 \text{ mm}^2$, which was chosen according to devices operating at around 5.0 GHz. The results of reflection coefficient (S_{11}) measurements are shown in Figure 9. S_{11} spectra for all samples showed minimal S_{11} values below -10 dB , which are required for a good antenna operation. In these conditions ($S_{11} < -10 \text{ dB}$), the antennas are well-matched and more than 90% of input power is accepted by the antenna to radiate [57].

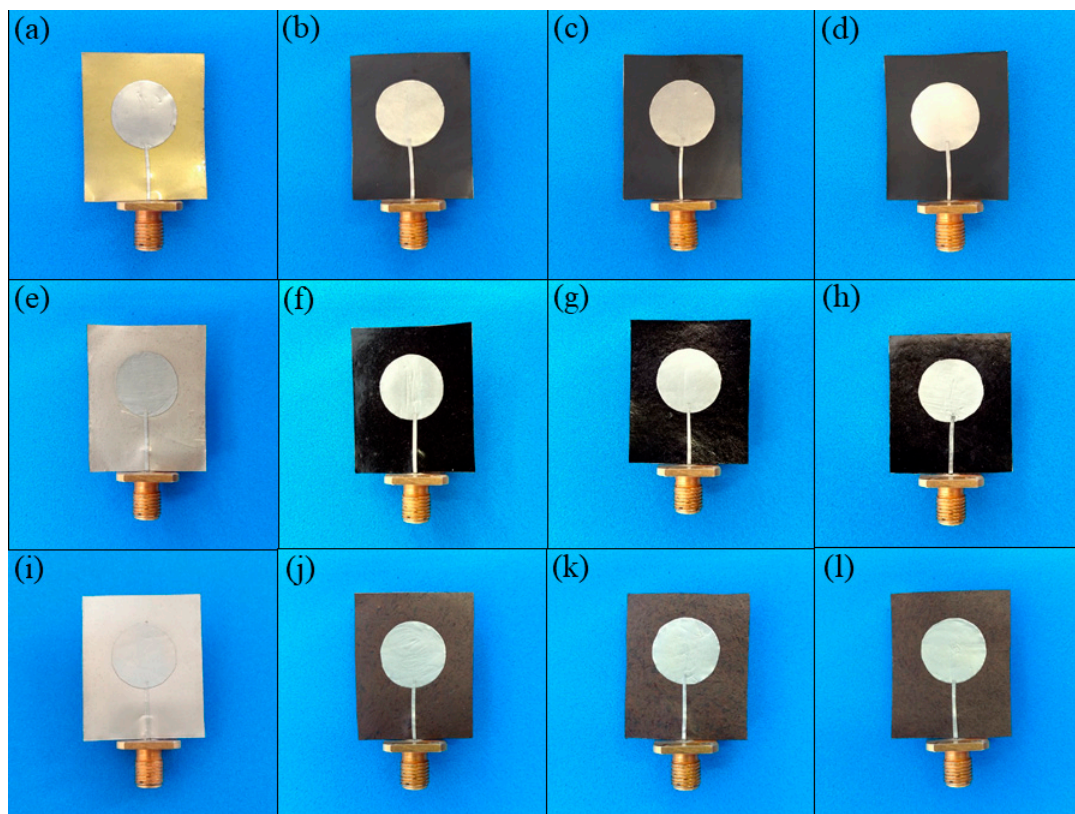


Figure 8. Microstrip antennas developed with substrates based on Ch (a–d, 0–80% of SPIONs, respectively), Col (e–h, 0–80%) and BC (i–l, 0–80%).

The operation frequencies (f_o), calculated and experimental obtained, as well as experimental bandwidths (BW), of all microstrip antennas are shown in Table 3. Experimental f_o values were acceptable according to values calculated by Equation (1), where c is the velocity of light in the vacuum, a is the patch diameter and h , μ' and ϵ' are the thickness, the magnetic permeability and dielectric permittivity of the substrate, respectively [54]. In order to simplify the calculations for these antennas, due to the μ' values at 5 GHz not being known, it was assumed that $\mu' = 1$.

$$f_o = \frac{1.8412c}{2\pi a \left\{ 1 + \frac{2h}{\pi a \mu' \epsilon'} \left[\ln\left(\frac{\pi a}{2h}\right) + 1.7726 \right] \right\}^{\frac{1}{2}} \sqrt{\mu' \epsilon'}} \quad (1)$$

Table 3. Calculated and experimental operating frequencies and bandwidths for prepared microstrip antennas.

| Samples | ϵ' (4.33 GHz) | f_o (GHz) Calc. | f_o (GHz) Exp. | Error (%) | BW (%) |
|---------|------------------------|-------------------|------------------|-----------|--------|
| Ch0 | 5.2 | 5.89 | 5.55 | 6.12 | 5.47 |
| Ch30 | 6.1 | 5.44 | 5.41 | 0.55 | 3.40 |
| Ch50 | 6.8 | 5.18 | 5.23 | 0.96 | 5.35 |
| Ch80 | 8.3 | 4.67 | 4.69 | 0.43 | 5.58 |
| Col0 | 5.9 | 5.55 | 5.44 | 2.02 | 6.36 |
| Col30 | 7.2 | 5.02 | 5.33 | 5.82 | 3.27 |
| Col50 | 7.5 | 4.90 | 5.03 | 2.58 | 4.81 |
| Col80 | 9.1 | 4.46 | 4.93 | 9.53 | 5.61 |
| BC0 | 6.7 | 5.20 | 5.18 | 0.39 | 5.57 |
| BC30 | 7.3 | 4.98 | 4.97 | 0.20 | 6.34 |
| BC50 | 7.5 | 4.92 | 4.72 | 4.24 | 5.65 |
| BC80 | 8.4 | 4.66 | 4.63 | 0.65 | 6.10 |

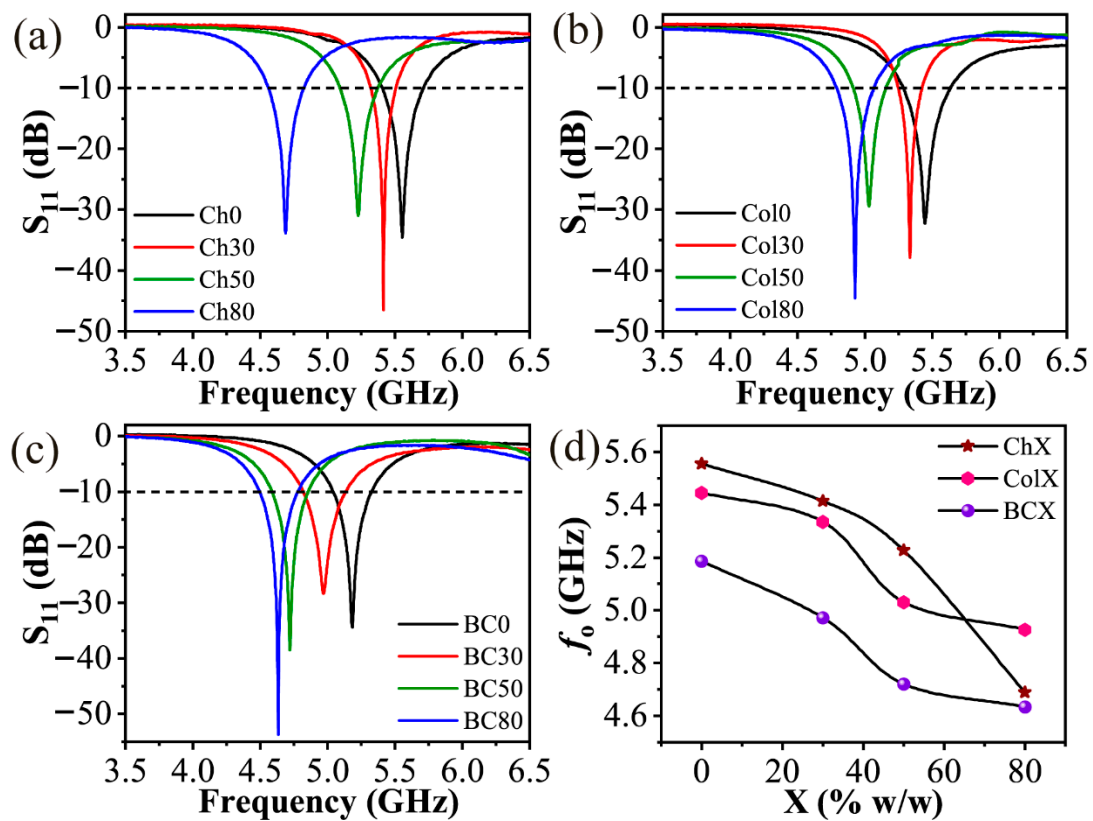


Figure 9. Measured reflection coefficient S_{11} of microstrip antennas prototypes of (a) Ch-based films (0–80% of SPIONs); (b) Col-based films (0–80% of SPIONs); and (c) BC-based films (0–80% of SPIONs). (d) Variation of operation frequency in function of the composition of microstrip substrate.

In circular microstrip antennas with thin substrates, two factors significantly affect f_0 , a and ϵ' , where f_0 is inversely proportional to $\sqrt{\epsilon'}$. The increase of SPIONs content in the composites results in higher values of ϵ' , consequently displacing f_0 of microstrips to lower values. Therefore, that behavior profile can provide a great possibility of miniaturization of the antennas. However, as shown in Table 3, some deviations from Equation (1) were obtained, which can be related to air gaps between substrate and ground plane and patch. Indeed, there might be some contribution of error patch cutting in these shifts.

Figure 9d shows f_0 values of antennas *versus* composition of their respective substrates in the composite film. Interestingly, it is possible to adjust the operation frequency of microstrips with the substrate content. For instance, a chitosan matrix showed the largest tunability with the composition, making it possible to work in f_0 from 5.55 to 4.69 GHz, while varying the SPIONs increment from 0 to 80%. Although collagen films have permittivity values in the range of chitosan films, a higher thickness variation could negatively contribute (with a higher h and lower f_0) to f_0 adjustability of collagen devices. Furthermore, according to dielectric characterization, chitosan composites presented the lowest losses, showing the most attractive profile as a substrate for applications in microwave technologies.

Usually, a frequency range, the so-called bandwidth (BW), is considered as being acceptable to antenna operation, maintaining its performance. Taking S_{11} values < -10 dB as a limit, the BW values of all prepared microstrip antennas are shown in Table 3. BW were calculated through Equation (2), where Δf is the difference (modulus) between the two frequencies at $S_{11} = -10$ dB, and f_0 is the frequency at lower S_{11} .

$$BW = \frac{\Delta f}{f_0} \quad (2)$$

Controversially, there was no significant reduction in BW values of the prototypes, related to the increase of ϵ' with the addition of SPIONs in the films. The increment of $\text{Fe}_3\text{O}_4@b\text{PEI}$ NPs provided a broader bandwidth for Ch and Col-based composites, which was associated to the increased permeability of these composites [58,59]. Interestingly, this behavior was not observed for BC-based films, showing broader BW when compared to pure BC film-form.

Herein, for microstrip antennas prototypes developed in this work, device miniaturization applications should be also considered for short-range wireless local area networks (WLANs), such as Wi-Fi, which operates at low (2.40–2.48 GHz) and high (5.15–5.8 GHz) frequencies ranges [60]. For operations at a higher frequency range, antenna devices can be developed using substrates based on chitosan films with up to 50% of SPIONs, collagen until 30% of filler and pure BC film-form. However, the inapplicability of the other biopolymer-based composites is not taken into consideration, since their properties can be adjusted with a magnetic field [61,62]. Another possibility is adjusting the dimensions of ground plane and patch of prototypes. Indeed, f_0 values of all composites are presented in the C band, which is used for other several applications.

Therefore, the proposed biopolymer-based composite films are applicable in a wide range of public safety communications and astronomy radio services [63]. However, composite films based on a chitosan matrix showed a greater profile for application in microwaves, as they presented lower dielectric losses and a better modulation of film properties with SPIONs weight percentages.

4. Conclusions

In summary, the addition of $\text{Fe}_3\text{O}_4@b\text{PEI}$ NPs to biopolymer matrices, chitosan, collagen and bacterial cellulose, allowed the obtaining of composites with good dispersion and homogeneity, which were well-characterized by SEM and Fe mapping involving EDS. In addition, the obtaining process of composites maintained the chemical integrity of polymer matrix, which was indicated by FTIR and XRD. TGA results also showed that at usual temperatures only water weight loss was observed, attesting to the thermal stability of synthesized composites.

The substrates showed ϵ' in the range of 2–12 at frequencies above 1 GHz, depending on the filler content in the matrix, which was interesting for application in devices such as microstrip antennas. Other than in cellulose composites, the substrates showed $\tan \delta$ decreasing with the frequency increasing, thereby indicating its most suitable application in high-frequency devices. In addition, all biocomposite films showed a superparamagnetic behavior, which is highly needed to avoid magnetic losses in antennas.

In this work, prototypes of microstrip antennas were obtained with appreciate return losses and bandwidths. In addition, the operating frequency of the devices were modulated merely by varying the substrate composition, while microstrips with chitosan-SPIONs substrates showed the best modulation capacity and the smallest $\tan \delta$. Therefore, the proposed biocomposite films are suitable candidates for application in the wireless communication of devices on the microwave frequency, since their eco-friendly and cheap processing provided good dielectric properties, apparent flexibility, lightness and biodegradability.

Supplementary Materials: The following are available online at <http://www.mdpi.com/2504-477X/4/4/144/s1>, Figure S1: Micrographics for all SPIONs-based biocomposites at high magnification, Figure S2: Micrographics of SPIONs-based biocomposite surfaces at low magnification and Figure S3: Fe mappings by EDS of SPIONs-based biocomposite surfaces.

Author Contributions: Conceptualization, F.L.d.M., D.M.A.N., M.d.S.M.d.S.F. and P.B.A.F.; methodology, F.L.d.M., M.d.L.L.R., H.L.S.L., D.M.A.N. and P.B.A.F.; software, F.L.d.M., M.A.S.d.S., D.V.M.P. and P.B.A.F.; validation, F.L.d.M., M.d.L.L.R., H.L.S.L. and M.A.S.d.S.; formal analysis, F.L.d.M., D.V.M.P. and P.B.A.F.; investigation, F.L.d.M., M.d.L.L.R., H.L.S.L., R.M.F. and M.A.S.d.S.; resources, F.L.d.M., M.d.L.L.R., H.L.S.L. and S.E.M.; data curation, F.L.d.M. and M.A.S.d.S.; writing—original draft preparation, F.L.d.M.; writing—review and editing, P.B.A.F. and L.M.U.D.F.; visualization, F.L.d.M., P.B.A.F. and L.M.U.D.F.; supervision, M.d.S.M.d.S.F., M.d.F.R. and M.A.S.d.S.; project administration, F.L.d.M. and P.B.A.F.; funding acquisition, P.B.A.F., M.d.F.R., M.d.S.M.d.S.F., A.S.B.S., S.E.M. and J.C.D. All authors have read and agreed to the published version of the manuscript.

Funding: This work was funded by the Brazilian agencies for scientific and technological development: CNPq (408790/2016-4), CAPES (Finance Code 001, PROEX 23038.000509/2020-82) and Funcap (PNE-0112-00048.01.00/16). Also, we had the financial support of Fondecyt n° 3170240, Fondecyt n° 1200782 and Conicyt Basal CEDENNA AFB180001 from Chile.

Acknowledgments: The authors would like to acknowledge Embrapa Agroindústria Tropical, Central Analítica-UFC/CT-INFRA/MCTI-SISNANO/Pró-Equipamentos and X-ray Diffraction Laboratory (UFC).

Conflicts of Interest: The authors declare no conflict of interest. The funders had no role in the design of the study; in the collection, analyses or interpretation of data; in the writing of the manuscript or in the decision to publish the results.

References

1. Rahman, A.; Islam, M.T.; Singh, M.J.; Misran, N. Sol-gel synthesis of transition-metal doped ferrite compounds with potential flexible, dielectric and electromagnetic properties. *RSC Adv.* **2016**, *6*, 84562–84572. [[CrossRef](#)]
2. Vural, M.; Crowgey, B.; Kempel, L.C.; Kofinas, P. Nanostructured flexible magneto-dielectrics for radio frequency applications. *J. Mater. Chem. C* **2014**, *2*, 756–763. [[CrossRef](#)]
3. Chen, Z.; Liu, Y.; Fang, L.; Jiang, P.; Huang, X. Role of reduced graphene oxide in dielectric enhancement of ferroelectric polymers composites. *Appl. Surf. Sci.* **2019**, *470*, 348–359. [[CrossRef](#)]
4. Xu, F.; Zhang, H.; Jin, L.; Li, Y.; Li, J.; Gan, G.; Wei, M.; Li, M.; Liao, Y. Controllably degradable transient electronic antennas based on water-soluble PVA/TiO₂ films. *J. Mater. Sci.* **2018**, *53*, 2638–2647. [[CrossRef](#)]
5. Varghese, J.; Dinesh, A.; Nair, R.; Mohanan, P.; Sebastian, M.T. Dielectric, thermal and mechanical properties of zirconium silicate reinforced high density polyethylene composites for antenna applications. *Phys. Chem. Chem. Phys.* **2015**, *17*, 14943–14950. [[CrossRef](#)]
6. Morales, C.; Dewdney, J.; Pal, S.; Skidmore, S.; Stojak, K.; Srikanth, H.; Weller, T.; Wang, J. Tunable Magneto-Dielectric Polymer Nanocomposites for Microwave Applications. *IEEE Trans. Microw. Theory Tech.* **2011**, *59*, 302–310. [[CrossRef](#)]
7. Sun, D.; Chen, F.; Gao, Y.; Huang, S.; Wang, Y. Polymer-derived SiCN ceramics as fillers for polymer composites with high dielectric constants. *J. Mater. Sci.* **2019**, *54*, 6982–6990. [[CrossRef](#)]
8. Sun, H.-S.; Chiu, Y.-C.; Chen, W.-C. Renewable polymeric materials for electronic applications. *Polym. J.* **2017**, *49*, 61–73. [[CrossRef](#)]
9. Ambikeswari, N.; Manivannan, S. Superior magnetodielectric properties of room temperature synthesized superparamagnetic cobalt ferrite—Graphene oxide composite. *J. Alloys Compd.* **2018**, *763*, 711–718. [[CrossRef](#)]
10. Syed Nasser, S.S.; Liu, W.; Chen, Z.N. Wide Bandwidth and Enhanced Gain of a Low-Profile Dipole Antenna Achieved by Integrated Suspended Metasurface. *IEEE Trans. Antennas Propag.* **2018**, *66*, 1540–1544. [[CrossRef](#)]
11. Alqadami, A.S.M.; Jamlos, M.F.; Lago, H.; Babarinde, O.J. Bandwidth enhancement of a microstrip antenna array using magneto-dielectric polymer substrate (PDMS-Fe₃O₄). In *Proceedings of the 2014 IEEE Symposium on Wireless Technology and Applications (ISWTA), Kota Kinabalu, Malaysia, 28 September–1 October 2014*; IEEE: Piscataway, NJ, USA, 2014; pp. 152–155.
12. Ali-zade, R.A. Influence of Magnetic Field on Dielectric Permittivity of Nanocomposites on the Base of Polymeric Matrix: Collagen, Polystyrene, and Magnetite Nanoparticles. *IEEE Trans. Magn.* **2015**, *51*, 1–8. [[CrossRef](#)]
13. Stojak, K.; Pal, S.; Srikanth, H.; Morales, C.; Dewdney, J.; Weller, T.; Wang, J. Polymer nanocomposites exhibiting magnetically tunable microwave properties. *Nanotechnology* **2011**, *22*, 135602. [[CrossRef](#)]
14. Mallmann, E.J.J.; Goes, J.C.; Figueiro, S.D.; Ricardo, N.M.P.S.; Denardin, J.C.; Sombra, A.S.B.; Maia, F.J.N.; Mazzeto, S.E.; Fechine, P.B.A. Microstructure and magneto-dielectric properties of the chitosan/gelatin-YIG biocomposites. *Express Polym. Lett.* **2011**, *5*, 1041–1049. [[CrossRef](#)]
15. Souza, N.D.G.; Freire, R.M.; Cunha, A.P.; Da Silva, M.A.S.; Mazzetto, S.E.; Sombra, A.S.B.; Denardin, J.C.; Ricardo, N.M.P.S.; Fechine, P.B.A. New magnetic nanobiocomposite based in galactomannan/glycerol and superparamagnetic nanoparticles. *Mater. Chem. Phys.* **2015**, *156*, 113–120. [[CrossRef](#)]
16. Figueiro, S.D.; Mallmann, E.J.J.; Góes, J.C.; Ricardo, N.M.P.S.; Denardin, J.C.; Sombra, A.S.B.; Fechine, P.B.A. New ferrimagnetic biocomposite film based in collagen and yttrium iron garnet. *Express Polym. Lett.* **2010**, *4*, 790–797. [[CrossRef](#)]

17. Gheorghiu, F.; Stanculescu, R.; Curecheriu, L.; Brunengo, E.; Stagnaro, P.; Tiron, V.; Postolache, P.; Buscaglia, M.T.; Mitoseriu, L. PVDF–ferrite composites with dual magneto-piezoelectric response for flexible electronics applications: Synthesis and functional properties. *J. Mater. Sci.* **2020**, *55*, 3926–3939. [[CrossRef](#)]
18. Castro, J.; Morales, C.; Weller, T.; Wang, J.; Srikanth, H. Synthesis and characterization of low-loss Fe₃O₄-PDMS magneto-dielectric polymer nanocomposites for RF applications. In *Proceedings of the WAMICON 2014, Tampa, FL, USA, 6 June 2014*; IEEE: Piscataway, NJ, USA, 2014; pp. 1–5.
19. Muhamad, W.A.W.; Ngah, R.; Jamlos, M.F.; Soh, P.J.; Jamlos, M.A.; Lago, H. Antenna array bandwidth enhancement using polymeric nanocomposite substrate. *Appl. Phys. A* **2016**, *122*, 426. [[CrossRef](#)]
20. Jafari-Soghieh, F.; Maleki, B.; Behniafar, H. Effect of dendrimer-functionalized magnetic iron oxide nanoparticles on improving thermal and mechanical properties of DGEBA/IPD epoxy networks. *High Perform. Polym.* **2019**, *31*, 24–31. [[CrossRef](#)]
21. Zhu, P.; Weng, L.; Zhang, X.; Wang, X.; Guan, L.; Liu, L. Graphene@poly(dopamine)-Ag core-shell nanoplatelets as fillers to enhance the dielectric performance of polymer composites. *J. Mater. Sci.* **2020**, 1–15. [[CrossRef](#)]
22. Sun, L.; Hou, H.; Li, B.; Zhang, Y. Characterization of acid- and pepsin-soluble collagen extracted from the skin of Nile tilapia (*Oreochromis niloticus*). *Int. J. Biol. Macromol.* **2017**, *99*, 8–14. [[CrossRef](#)]
23. Lima, H.L.S.; Gonçalves, C.; Cerqueira, M.Â.; Do Nascimento, E.S.; Gama, M.F.; Rosa, M.F.; Borges, M.d.F.; Pastrana, L.M.; Brígida, A.I.S. Bacterial cellulose nanofiber-based films incorporating gelatin hydrolysate from tilapia skin: Production, characterization and cytotoxicity assessment. *Cellulose* **2018**, *25*, 6011–6029. [[CrossRef](#)]
24. Hestrin, S.; Schramm, M. Synthesis of cellulose by *Acetobacter xylinum*. II. Preparation of freeze-dried cells capable of polymerizing glucose to cellulose. *Biochem. J.* **1954**, *58*, 345–352. [[CrossRef](#)]
25. Andrade Neto, D.M.; Freire, R.M.; Gallo, J.; Freire, T.M.; Queiroz, D.C.; Ricardo, N.M.P.S.; Vasconcelos, I.F.; Mele, G.; Carbone, L.; Mazzetto, S.E.; et al. Rapid Sonochemical Approach Produces Functionalized Fe₃O₄ Nanoparticles with Excellent Magnetic, Colloidal, and Relaxivity Properties for MRI Application. *J. Phys. Chem. C* **2017**, *121*, 24206–24222. [[CrossRef](#)]
26. Kent, G. An Evanescent-Mode Tester for Ceramic Dielectric Substrates. *IEEE Trans. Microw. Theory Tech.* **1988**, *36*, 1451–1454. [[CrossRef](#)]
27. Sebastian, M.T.; Silva, M.A.S.; Sombra, A.S.B. Measurement of Microwave Dielectric Properties and Factors Affecting Them. In *Microwave Materials and Applications*; Sebastian, M.T., Jantunen, H., Ubic, R., Eds.; John Wiley & Sons, Ltd.: Chichester, UK, 2017; pp. 1–51. ISBN 9781119208549.
28. Cobos, M.; González, B.; Fernández, M.J.; Fernández, M.D. Chitosan-graphene oxide nanocomposites: Effect of graphene oxide nanosheets and glycerol plasticizer on thermal and mechanical properties. *J. Appl. Polym. Sci.* **2017**, *134*, 45092. [[CrossRef](#)]
29. Guerrero, P.; Muxika, A.; Zarandona, I.; De la Caba, K. Crosslinking of chitosan films processed by compression molding. *Carbohydr. Polym.* **2019**, *206*, 820–826. [[CrossRef](#)]
30. Giannakas, A.; Grigoriadi, K.; Leontiou, A.; Barkoula, N.-M.; Ladavos, A. Preparation, characterization, mechanical and barrier properties investigation of chitosan–clay nanocomposites. *Carbohydr. Polym.* **2014**, *108*, 103–111. [[CrossRef](#)]
31. Segal, L.; Creely, J.J.; Martin, A.E.; Conrad, C.M. An Empirical Method for Estimating the Degree of Crystallinity of Native Cellulose Using the X-Ray Diffractometer. *Text. Res. J.* **1959**, *29*, 786–794. [[CrossRef](#)]
32. Wang, L.; Schütz, C.; Salazar-Alvarez, G.; Titirici, M.-M. Carbon aerogels from bacterial nanocellulose as anodes for lithium ion batteries. *RSC Adv.* **2014**, *4*, 17549–17554. [[CrossRef](#)]
33. Tabarsa, T.; Sheykhnazari, S.; Ashori, A.; Mashkour, M.; Khazaeian, A. Preparation and characterization of reinforced papers using nano bacterial cellulose. *Int. J. Biol. Macromol.* **2017**, *101*, 334–340. [[CrossRef](#)]
34. Wada, M.; Okano, T. Localization of I α and I β phases in algal cellulose revealed by acid treatments. *Cellulose* **2001**, *8*, 183–188. [[CrossRef](#)]
35. Jin, E.; Guo, J.; Yang, F.; Zhu, Y.; Song, J.; Jin, Y.; Rojas, O.J. On the polymorphic and morphological changes of cellulose nanocrystals (CNC-I) upon mercerization and conversion to CNC-II. *Carbohydr. Polym.* **2016**, *143*, 327–335. [[CrossRef](#)]
36. Kloster, G.A.; Marcovich, N.E.; Mosiewicki, M.A. Composite films based on chitosan and nanomagnetite. *Eur. Polym. J.* **2015**, *66*, 386–396. [[CrossRef](#)]

37. Matet, M.; Heuzey, M.-C.; Pollet, E.; Aji, A.; Avérous, L. Innovative thermoplastic chitosan obtained by thermo-mechanical mixing with polyol plasticizers. *Carbohydr. Polym.* **2013**, *95*, 241–251. [[CrossRef](#)] [[PubMed](#)]
38. De Moraes Lima, M.; Bianchini, D.; Guerra Dias, A.; Da Rosa Zavareze, E.; Prentice, C.; Da Silveira Moreira, A. Biodegradable films based on chitosan, xanthan gum, and fish protein hydrolysate. *J. Appl. Polym. Sci.* **2017**, *134*. [[CrossRef](#)]
39. Khoury, C.; Gazit, O.M. Self-Organized Porous Titanium-Chitosan Hybrid Materials with Tunable Functions. *ChemNanoMat* **2018**, *4*, 353–360. [[CrossRef](#)]
40. Freire, T.M.; Dutra, L.M.U.; Queiroz, D.C.; Ricardo, N.M.P.S.; Barreto, K.; Denardin, J.C.; Wurm, F.R.; Sousa, C.P.; Correia, A.N.; De Lima-Neto, P.; et al. Fast ultrasound assisted synthesis of chitosan-based magnetite nanocomposites as a modified electrode sensor. *Carbohydr. Polym.* **2016**, *151*, 760–769. [[CrossRef](#)] [[PubMed](#)]
41. Chen, J.; Li, L.; Yi, R.; Xu, N.; Gao, R.; Hong, B. Extraction and characterization of acid-soluble collagen from scales and skin of tilapia (*Oreochromis niloticus*). *LWT Food Sci. Technol.* **2016**, *66*, 453–459. [[CrossRef](#)]
42. El-Rashidy, A.A.; Gad, A.; Abu-Hussein, A.E.-H.G.; Habib, S.I.; Badr, N.A.; Hashem, A.A. Chemical and biological evaluation of Egyptian Nile Tilapia (*Oreochromis niloticus*) fish scale collagen. *Int. J. Biol. Macromol.* **2015**, *79*, 618–626. [[CrossRef](#)]
43. Chen, J.-H.; Liu, J.-G.; Su, Y.-Q.; Xu, Z.-H.; Li, M.-C.; Ying, R.-F.; Wu, J.-Q. Preparation and properties of microfibrillated cellulose with different carboxyethyl content. *Carbohydr. Polym.* **2019**, *206*, 616–624. [[CrossRef](#)]
44. Gea, S.; Reynolds, C.T.; Roohpour, N.; Wirjosentono, B.; Soykeabkaew, N.; Bilotti, E.; Peijs, T. Investigation into the structural, morphological, mechanical and thermal behaviour of bacterial cellulose after a two-step purification process. *Bioresour. Technol.* **2011**, *102*, 9105–9110. [[CrossRef](#)] [[PubMed](#)]
45. Li, H.; Jiang, M.; Dong, L.; Xie, H.; Xiong, C. Particle Size Dependence of the Dielectric Properties of Polyvinylidene Fluoride/Silver Composites. *J. Macromol. Sci. Part B* **2013**, *52*, 1073–1081. [[CrossRef](#)]
46. Zhao, C.; Wei, X.; Huang, Y.; Ma, J.; Cao, K.; Chang, G.; Yang, J. Preparation and unique dielectric properties of nanoporous materials with well-controlled closed-nanopores. *Phys. Chem. Chem. Phys.* **2016**, *18*, 19183–19193. [[CrossRef](#)] [[PubMed](#)]
47. Iswariya, S.; Bhanukeerthi, A.V.; Velswamy, P.; Uma, T.S.; Perumal, P.T. Design and development of a piscine collagen blended pullulan hydrogel for skin tissue engineering. *RSC Adv.* **2016**, *6*, 57863–57871. [[CrossRef](#)]
48. Maria, V.D.; Bernal, C.; Francois, N.J.; Francois, N.J. Development of Biodegradable Films Based on Chitosan/Glycerol Blends Suitable for Biomedical Applications. *J. Tissue Sci. Eng.* **2016**, *7*. [[CrossRef](#)]
49. Li, J.; Li, G. The thermal behavior of collagen in solution: Effect of glycerol and 2-propanol. *Int. J. Biol. Macromol.* **2011**, *48*, 364–368. [[CrossRef](#)]
50. Augustine, R.; Kalappura, U.G.; Laheurte, J.-M.; Mathew, K.T. Biocompatibility study of beta tricalcium phosphate bioceramics and chitosan biopolymer and their use as phantoms for medical imaging applications. *Microw. Opt. Technol. Lett.* **2009**, *51*, 2923–2927. [[CrossRef](#)]
51. Da Silva, A.L.; Da Silva, L.R.R.; Camargo, I.d.A.; Agostini, D.L.d.S.; Denardin, J.C.; Rosa, D.d.S.; Mele, G.; De Oliveira, D.L.V.; Fechine, P.B.A.; Mazzetto, S.E. Superparamagnetic nano-biocomposites for application as dielectric resonator antennas. *Mater. Chem. Phys.* **2017**, *185*, 104–113. [[CrossRef](#)]
52. Vikram Babu, B.; Vijaya Babu, K.; Tewodros Aregai, G.; Seeta Devi, L.; Madhavi Latha, B.; Sushma Reddi, M.; Samatha, K.; Veeraiah, V. Structural and electrical properties of Li₄Ti₅O₁₂ anode material for lithium-ion batteries. *Results Phys.* **2018**, *9*, 284–289. [[CrossRef](#)]
53. Bibikov, S.B.; Kulikovskij, E.I.; Sharafiev, R.S.; Bychkova, A.V.; Ol'khov, A.A. Nanocomposites for antenna-feeder systems. In *Proceedings of the 2013 IX International Conference on Antenna Theory and Techniques, Odesa, Ukraine, 16–20 September 2013*; IEEE: Piscataway, NJ, USA, 2013; pp. 500–502.
54. Balanis, C.A. *Antenna Theory: Analysis and Design*, 3rd ed.; John Wiley & Sons: Hoboken, NJ, USA, 2005; ISBN 0-471-66782-X.
55. Melone, L.; Rossi, B.; Pastori, N.; Panzeri, W.; Mele, A.; Punta, C. TEMPO-Oxidized Cellulose Cross-Linked with Branched Polyethyleneimine: Nanostructured Adsorbent Sponges for Water Remediation. *Chempluschem* **2015**, *80*, 1408–1415. [[CrossRef](#)]
56. Nunes, W.C.; Cebollada, F.; Knobel, M.; Zanchet, D. Effects of dipolar interactions on the magnetic properties of γ -Fe₂O₃ nanoparticles in the blocked state. *J. Appl. Phys.* **2006**, *99*, 08N705. [[CrossRef](#)]

57. Tung, T.T.; Chen, S.J.; Fumeaux, C.; Losic, D. Scalable realization of conductive graphene films for high-efficiency microwave antennas. *J. Mater. Chem. C* **2016**, *4*, 10620–10624. [[CrossRef](#)]
58. Yousefi, L.; Mohajer-Iravani, B.; Ramahi, O.M. Enhanced bandwidth artificial magnetic ground plane for low-profile antennas. *IEEE Antennas Wirel. Propag. Lett.* **2007**, *6*, 289–292. [[CrossRef](#)]
59. Sharifi, M.; Rezaei, P. Designing and modeling of compact microstrip antennas using new nanocomposite materials. *ARPJ. Eng. Appl. Sci.* **2017**, *12*, 6825–6833.
60. Jose, S.K.; Suganthi, S. Circular-Rectangular Microstrip Antenna for Wireless Applications. *Int. J. Microw. Appl.* **2015**, *4*, 6–10.
61. De Moraes, J.E.V.; De Castro, A.J.N.; Oliveira, R.G.M.; Do Carmo, F.F.; Sales, A.J.M.; Sales, J.C.; Silva, M.A.S.; Gouveia, D.X.; Costa, M.M.; Rodrigues, A.R.; et al. Magneto Tuning of a Ferrite Dielectric Resonator Antenna Based on LiFe₅O₈ Matrix. *J. Electron. Mater.* **2018**, *47*, 3829–3835. [[CrossRef](#)]
62. Fechine, P.B.A.; Moretzsohn, R.S.T.; Costa, R.C.S.; Derov, J.; Stewart, J.W.; Drehman, A.J.; Junqueira, C.; Sombra, A.S.B. Magneto-dielectric properties of the Y₃Fe₅O₁₂ and Gd₃Fe₅O₁₂ dielectric ferrite resonator antennas. *Microw. Opt. Technol. Lett.* **2008**, *50*, 2852–2857. [[CrossRef](#)]
63. Bhardwaj, D.; Saraswat, S.; Gulati, G.; Shekhar, S.; Joshi, K.; Sharma, K. Dual band multi frequency rectangular patch microstrip antenna with flyswatter shaped slot for wireless systems. In *Proceedings of the AIP Conference Proceedings, Rajasthan, India, 18–20 October 2015*; AIP Publishing: Melville, NY, USA, 2016; Volume 1715, p. 020033.



© 2020 by the authors. Licensee MDPI, Basel, Switzerland. This article is an open access article distributed under the terms and conditions of the Creative Commons Attribution (CC BY) license (<http://creativecommons.org/licenses/by/4.0/>).